University of Glasgow

Phillips, D.B., Gibson, G.M., Bowman, R., Padgett, M.J., Hanna, S., Carberry, D.M., Miles, M.J., and Simpson, S.H. (2012) *An optically actuated surface scanning probe.* Optics Express, 20 (28). p. 29679. ISSN 1094-4087

Copyright © 2012 Optical Society of America

A copy can be downloaded for personal non-commercial research or study, without prior permission or charge

The content must not be changed in any way or reproduced in any format or medium without the formal permission of the copyright holder(s)

http://eprints.gla.ac.uk/73836/

Deposited on: 9 January 2013

Enlighten – Research publications by members of the University of Glasgow
http://eprints.gla.ac.uk

An optically actuated surface scanning probe

D. B. Phillips,[1]* G. M. Gibson,[2] R. Bowman,[2] M. J. Padgett,[2] S. Hanna,[1] D. M. Carberry,[1] M. J. Miles,[1] and S. H. Simpson[1]

[1] *H. H. Wills Physics Laboratories, University of Bristol, Bristol, England, UK*
[2] *SUPA, Department of Physics and Astronomy, University of Glasgow, Glasgow, Scotland, UK*
* *dave.phillips@bristol.ac.uk*

Abstract: We demonstrate the use of an extended, optically trapped probe that is capable of imaging surface topography with nanometre precision, whilst applying ultra-low, femto-Newton sized forces. This degree of precision and sensitivity is acquired through three distinct strategies. First, the probe itself is shaped in such a way as to soften the trap along the sensing axis and stiffen it in transverse directions. Next, these characteristics are enhanced by selectively position clamping independent motions of the probe. Finally, force clamping is used to refine the surface contact response. Detailed analyses are presented for each of these mechanisms. To test our sensor, we scan it laterally over a calibration sample consisting of a series of graduated steps, and demonstrate a height resolution of ~ 11 nm. Using equipartition theory, we estimate that an average force of only ~ 140 fN is exerted on the sample during the scan, making this technique ideal for the investigation of delicate biological samples.

© 2012 Optical Society of America

OCIS codes: (140.7010) Laser trapping; (170.4520) Optical confinement and manipulation.

References and links

1. A. Ashkin, J. M. Dziedzic, J. E. Bjorkholm, and S. Chu, "Observation of A Single-beam Gradient Force Optical Trap For Dielectric Particles," Opt. Lett. **11**(5), 288–290 (1986).
2. A. Pralle, M. Prummer, E. L. Florin, E. H. K. Stelzer, and J. K. H. Horber, "Three-dimensional high-resolution particle tracking for optical tweezers by forward scattered light," Microsc. Res. Techniq. **44**(5), 378–386 (1999).
3. A. Rohrbach, C. Tischer, D. Neumayer, E. L. Florin, and E. H. K. Stelzer, "Trapping and tracking a local probe with a photonic force microscope," Rev. Sci. Instrum. **75**(6), 2197–2210 (2004).
4. E. L. Florin, A. Pralle, J. K. H. Horber, and E. H. K. Stelzer, "Photonic force microscope based on optical tweezers and two-photon excitation for biological applications," J. Struct. Biol. **119**(2), 202–211 (1997).
5. J. E. Molloy, J. E. Burns, J. Kendrick-Jones, R. T. Tregear, and D. C. S. White, "Movement and Force Produced By A Single Myosin Head," Nature **378**(6553), 209–212 (1995).
6. P. C. Seitz, E. H. K. Stelzer, and A. Rohrbach, "Interferometric tracking of optically trapped probes behind structured surfaces: a phase correction method," Appl. Optics **45**(28), 7309–7315 (2006).
7. J. Gluckstad, A. R. Banas, T. Aabo, and D. Palima, "Structure-mediated micro-to-nano coupling using sculpted light and matter," in *Proc. SPIE.*, **8424**, 84241L (2012).
8. D. Grier, "A revolution in optical manipulation," Nature **424**(6950), 810–816 (2003).
9. P. J. Rodrigo, I. R. Perch-Nielsen, C. A. Alonzo, and J. Gluckstad, "GPC-based optical micromanipulation in 3D real-time using a single spatial light modulator," Opt. Express **14**(26), 13107–13112 (2006).
10. D. Palima, A. R. Banas, G. Vizsnyiczai, L. Kelemen, P. Ormos, and J. Gluckstad, "Wave-guided optical waveguides," Opt. Express **20**(3), 2004–2014 (2012).
11. S. H. Simpson and S. Hanna, "Holographic optical trapping of microrods and nanowires," J. Opt. Soc. Am. A **27**(6), 1255–1264 (2010).

#179434 - $15.00 USD Received 7 Nov 2012; revised 13 Dec 2012; accepted 13 Dec 2012; published 20 Dec 2012

12. D. B. Phillips, D. M. Carberry, S. H. Simpson, H. Schaefer, M. Steinhart, R. Bowman, G. M. Gibson, M. J. Padgett, S. Hanna, and M. J. Miles, "Optimizing the optical trapping stiffness of holographically trapped microrods using high-speed video tracking," J. Opt. **13**(4), 044023 (2011).
13. S. H. Simpson and S. Hanna, "Optical trapping of microrods: variation with size and refractive index," J. Opt. Soc. Am. A **28**(5), 850–858 (2011).
14. A. La Porta and M. D. Wang, "Optical torque wrench: Angular trapping, rotation, and torque detection of quartz microparticles," Phys. Rev. Lett. **92**(19), 190801 (2004).
15. O. M. Marago, P. H. Jones, F. Bonaccorso, V. Scardaci, P. G. Gucciardi, A. G. Rozhin, and A. C. Ferrari, "Femtonewton Force Sensing with Optically Trapped Nanotubes," Nano Lett. **8**(10), 3211–3216 (2008).
16. R. Di Leonardo, E. Cammarota, G. Bolognesi, H. Schaefer, and M. Steinhart, "Three-Dimensional to Two-Dimensional Crossover in the Hydrodynamic Interactions between Micron-Scale Rods," Phys. Rev. Lett. **107**(4), 044501 (2011).
17. P. J. Reece, W. J. Toe, F. Wang, S. Paiman, Q. Gao, H. H. Tan, and C. Jagadish, "Characterization of Semiconductor Nanowires Using Optical Tweezers," Nano Lett. **11**(6), 2375–2381 (2011).
18. M. E. J. Friese, A. G. Truscott, H. Rubinsztein-Dunlop, and N. R. Heckenberg, "Three-dimensional imaging with optical tweezers," Appl. Opt. **38**(31), 6597–6603 (1999).
19. D. B. Phillips, J. A. Grieve, S. N. Olof, S. J. Kocher, R. Bowman, M. J. Padgett, M. J. Miles, and D. M. Carberry, "Surface imaging using holographic optical tweezers," Nanotechnol. **22**(28), 285503 (2011).
20. D. B. Phillips, S. H. Simpson, J. A. Grieve, G. M. Gibson, R. Bowman, M. J. Padgett, M. J. Miles, and D. M. Carberry, "Position clamping of optically trapped microscopic non-spherical probes," Opt. Express **19**(21), 20622–20627 (2011).
21. D. B. Phillips, S. H. Simpson, J. A. Grieve, R. Bowman, G. M. Gibson, M. J. Padgett, J. G. Rarity, S. Hanna, M. J. Miles, and D. M. Carberry, "Force sensing with a shaped dielectric micro-tool," Europhys. Lett. **99**, 58004 (2012).
22. G. Gibson, D. M. Carberry, G. Whyte, J. Leach, J. Courtial, J. C. Jackson, D. Robert, M. Miles, and M. Padgett, "Holographic assembly workstation for optical manipulation," J. Opt A-Pure Appl. Op. **10**(4), 044009 (2008).
23. D. Preece, R. Bowman, A. Linnenberger, G. Gibson, S. Serati, and M. Padgett, "Increasing trap stiffness with position clamping in holographic optical tweezers," Opt. Express **17**(25), 22718–22725 (2009).
24. R. Bowman, D. Preece, G. Gibson, and M. Padgett, "Stereoscopic particle tracking for 3D touch, vision and closed-loop control in optical tweezers," J. Opt. **13**(4), 044003 (2011).
25. G. Gibson, J. Leach, S. Keen, A. J. Wright and M. Padgett, "Measuring the accuracy of particle position and force in optical tweezers using high-speed video microscopy," Opt. Express **16**(19), 14561–14570 (2008).
26. S. H. Simpson and S. Hanna, "First-order nonconservative motion of optically trapped nonspherical particles," Phys. Rev. E **82**(3), 031141 (2010).
27. S. H. Simpson and S. Hanna, "Thermal motion of a holographically trapped SPM-like probe," Nanotechnol. **20**(39), 395710 (2009).
28. K. D. Wulff, D. G. Cole, and R. L. Clark, "Servo control of an optical trap," Appl. Opt. **46**(22), 4923–4931 (2007).
29. A. Rohrbach, "Switching and measuring a force of 25 femtoNewtons with an optical trap," Opt. Express **13**(24), 9695–9701 (2005).
30. M. R. Pollard, S. W. Botchway, B. Chichkov, E. Freeman, R. N. J. Halsall, D. W. K. Jenkins, I. Loader, A. Ovsianikov, A. W. Parker, R. Stevens, R. Turchetta, A. D. Ward, and M. Towrie, "Optically trapped probes with nanometer-scale tips for femto-Newton force measurement," New J. Phys. **12**, 1130560 (2010).
31. C. Agnew, E. Borodina, N. R. Zaccai, R. Conners, N. M. Burton, J. A. Vicary, D. K. Cole, M. Antognozzi, M. Virji, and R. L. Brady, "Correlation of in situ mechanosensitive responses of the Moraxella catarrhalis adhesin UspA1 with fibronectin and receptor CEACAM1 binding," P. Natl. Acad. Sci. USA **108**(37), 15174–15178 (2011).
32. J. B. Wills, J. R. Butler, J. Palmer, and J. P. Reid, "Using optical landscapes to control, direct and isolate aerosol particles," Phys. Chem. Chem. Phys. **11**(36), 8015–8020 (2009).
33. M. P. Lee, A. Curran, G. M. Gibson, M. Tassieri, N. R. Heckenberg, and M. J. Padgett, "Optical shield: measuring viscosity of turbid fluids using optical tweezers," Opt. Express **20**(11), 12127–12132 (2012).

1. Introduction

Optical tweezers use the high-intensity gradients produced in a tightly focused laser beam to trap micron-sized dielectric particles in three dimensions [1]. Particles trapped in a fluid are subject to Brownian motion, which causes them to explore a region around their equilibrium position, referred to here as the *thermal volume*. A sample which encroaches on the thermal volume of the probe further restricts its motion and, in doing so, the surface topography is revealed. Conventionally, this approach makes use of spheres of sub-wavelength dimensions held

#179434 - $15.00 USD Received 7 Nov 2012; revised 13 Dec 2012; accepted 13 Dec 2012; published 20 Dec 2012
(C) 2012 OSA

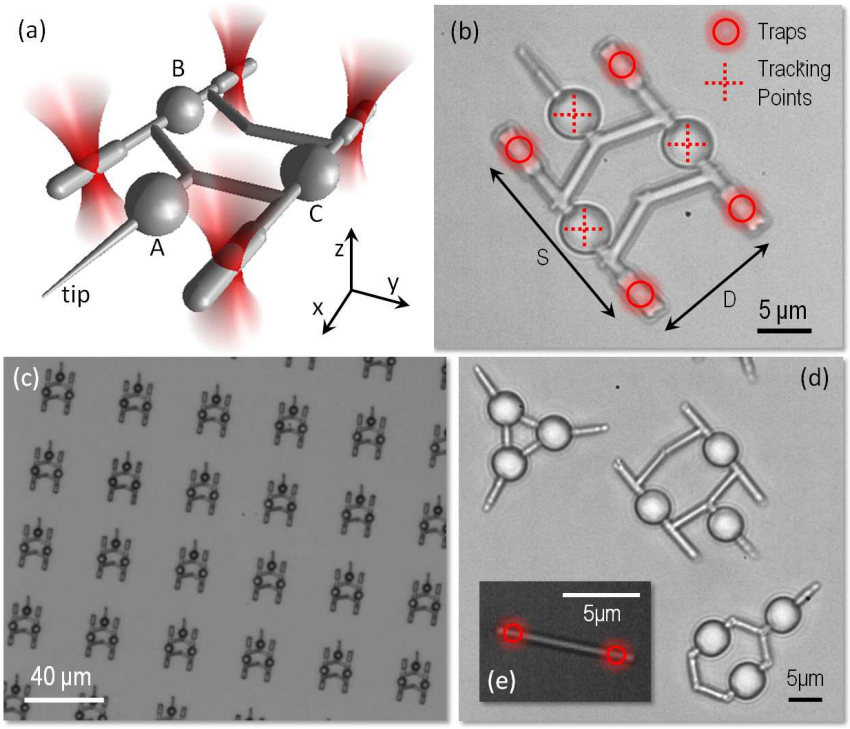

Fig. 1. (a) A rendering of our probe design showing the four cylindrical trapping handles. The axes indicate the probe *equilibrium frame* (see Appendix), the origin of which is at the averaged position of the three tracking spheres. The sensing axis is parallel to x. (b) An optical image of an optically trapped probe. (c) An array of micro-tools on a glass surface before they are transferred into a sample cell. Direct laser writing provides a simple and flexible technique to fabricate arbitrary probe geometries, (d) shows some examples of alternate probe designs in solution. (e) An optical image of a micro-rod held with its long axis parallel to the focal plane using two optical traps, providing the inspiration for our choice of probe geometry.

in Gaussian beams and is referred to as Photonic Force Microscopy (PFM) [2]. While highly successful in many applications [3–5], PFM has some drawbacks - the direct laser illumination of samples can be damaging to sensitive biological specimens, and it is less effective in optically dense environments where samples are likely to cause beam interference or occlusion. Altering the optical field in this unknown manner influences the optical forces acting on the particle and changes the thermal volume in a way that is difficult to decouple from the effects of the sample surface itself. It can also introduce errors into the measured position of the probe. Seitz et al. have investigated the effect of phase disturbances, introduced by surface structures, on the measured position (recorded using back focal plane interferometry) of an optically trapped microsphere [6]. They describe a method to correct for the presence of arbitrarily shaped scatterers with phase shifts comparable in magnitude to that of the probe by performing a pre-calibration step.

A different strategy is the use of an extended particle as a probe, which allows the trapping beams and probe tracking to be removed from the sample interface, enabling investigation of strongly scattering samples, without the need for a pre-calibration step. Such a probe also introduces new advantages, for example, the orientation, as well as the position of a non-spherical

#179434 - $15.00 USD Received 7 Nov 2012; revised 13 Dec 2012; accepted 13 Dec 2012; published 20 Dec 2012
(C) 2012 OSA

object can be controlled by dynamically reconfigurable traps. This permits control to be exerted over an arbitrarily sharp tip, giving rise to true *structure mediated micro-nano coupling* [7].

The development of techniques to generate and reconfigure multiple optical traps, such as holographic optical tweezers [8] and the generalised phase contrast method [9], have enabled trapping and video-rate control of structures more complex than a simple sphere [10]. The thermal motion of an optically trapped particle depends upon both its optical environment, and its geometry and composition. For example, optically trapped micro-rods, held with their long axis parallel to the microscope focal plane using two optical traps (as shown in Fig. 1(e)), have a trapping stiffness that is strongly dependent upon the separation of the trapping beams (optical environment) [11, 12], and the size, aspect ratio, and refractive index of the micro-rod (geometry and composition) [13]. In particular, the translational stiffness of the trap in the direction parallel to the long axis of the micro-rod can be greatly reduced by positioning the trapping beams well within the ends of the rod, whilst leaving the stiffness in other directions relatively unchanged. This is a useful property, allowing the sensitivity of the system parallel to the micro-rods long axis, the *sensing axis* (the direction in which forces are predominantly to be measured), to be tuned by adjusting the relative trap positions, with minimal effect on the *pointing precision* (the stiffness of the trap in directions transverse to the sensing direction, i.e. the precision with which the sensing element can be positioned). Increased attention has recently been directed towards the optical trapping and control of micro- and nano-rods, not only for their applications in high precision force and torque sensing [14, 15], but also in order to investigate their properties [16], and their potential in device fabrication [17].

In the following study, we investigate the use of a bespoke dielectric particle, fabricated using two photon polymerisation (Fig. 1), as a probe to investigate surface topography. This combines the ultra low force capabilities of optical tweezers with a scanning probe approach [18, 19]. We wish to measure the topography with high spatial resolution, whilst minimising the force applied to the surface. The latter condition being especially important in the context of soft biological samples, where we imagine our technique will be most beneficial. We use three methods to modify our probe's behaviour to best achieve this goal: handle shaping, position clamping, and force clamping. First, the handle shape is modified to generate a trapping stiffness anisotropy so that the probe is softly trapped along its sensing axis (and therefore highly sensitive to low forces), but stiffly trapped in the others (and so retains a good pointing precision). To achieve this, the probe handles are cylindrically shaped, inducing a trapping behaviour mimicking that of a multiply optically trapped micro-rod (Fig. 1(e)) [11, 12]. Incorporating this property into our micro-tool enables the probe's sensitivity and tip pointing precision to be controlled by varying the relative positions of the trapping beams. Next, trap anisotropy is further refined by position clamping specific modes of the probe's motion [20]. Finally, force clamping ensures the exertion of a constant force on a sample during a scan. By scanning our probe over a test sample consisting of a series of graduated steps, we demonstrate that this technique has a spatial resolution of ~ 11 nm along the sensing axis and applies an average force of only 140 fN normal to the sample, making it ideal for examining soft biological specimens that would otherwise be deformed and possibly damaged.

2. Methods

2.1. Probe fabrication

Figures 1(a) and (b) show the geometry of the probes demonstrated in this work. A probe is controlled using four holographically generated optical traps, each focused on a trapping handle formed from a right circular cylinder, 6 μm in length, and 2 μm in diameter. Three 5 μm diameter spheres serve as tracking points for stereo microscopic tracking (described in Section 2.2). The probe tip extends forward beyond the front most trapping handles to access

#179434 - $15.00 USD Received 7 Nov 2012; revised 13 Dec 2012; accepted 13 Dec 2012; published 20 Dec 2012
(C) 2012 OSA

the sample surface; it is 10 μm in length and tapers to a radius of curvature of 100 nm laterally and 300 nm vertically. Our probes are fabricated using a commercially available 3D direct write laser lithography system (Nanoscribe Photonic Professional), using a laser beam wavelength of 780 nm [21]. They are manufactured in batches of $\sim$100 (Fig. 1(c)), and dispersed into an aqueous solution of deionised water and 0.5 % *TWEEN 20* surfactant, with a typical transfer efficiency of $\sim$80 %, resulting in high numbers of probes in the required sample cell (Fig. 1(d)).

2.2. Probe control and measurement

The micro-tools are trapped and controlled using holographic optical tweezers. Our system is similar to that described in [22], designed around a commercially available inverted microscope (Axiovert 200, Zeiss). A 4 W 800 nm wavelength laser beam, generated by a titanium sapphire ring laser (899, Coherent) pumped by a solid state laser (Verdi-V18, Coherent) is expanded to fill an electrically addressed spatial light modulator (P512-0785, Boulder Nonlinear Systems) controlled using a LabVIEW (National Instruments) interface, with each hologram calculation performed on a PC graphics card (nVidia, Quadro FX 5600) in under 1 ms [23]. The beam is then passed through a polarising beam splitter and imaged onto the back aperture of an objective lens (1.3 NA 100 $\times$ Plan-Neufluar, Zeiss). This simultaneously focuses the trapping beam creating the optical traps, and images the sample. Approximately 40% of the laser beam's power is passed by the objective, and is shared between the traps. Movement of the field of view around the sample is achieved with a motorized *x-y* stage (MS2000, ASI) and a piezo-electric objective focussing system (Mipos 140 PL, Piezosystem Jena).

Three dimensional particle tracking is achieved using a high numerical aperture stereoscopic imaging system similar to that described in [24]. This provides two views of the sample from different directions, 60° apart. 'Left eye' and 'Right eye' views are imaged adjacently onto a high speed CMOS camera (Eo Sens MC 1362, Mikrotron). Two dimensional centre of symmetry tracking of a spherical particle's position in each image is combined using parallax to find its three dimensional location. Rigid transformations are used to determine the position and orientation of the extended probe from the three dimensional position of each of the three tracking spheres (see Appendix for more detail). The generalised coordinates $\mathbf{q} = [\mathbf{r}, \theta]$ describe the probe's instantaneous (i.e. measured from a single camera frame) displacement, $\mathbf{r} = [x, y, z]$, and rotation, $\theta = [\theta_x, \theta_y, \theta_z]$, relative to its equilibrium trapping position and orientation (the equilibrium frame is defined in Fig. 1(a)). The probe configuration is determined in real-time, at up to 1kHz, with image processing and coordinate calculation performed and displayed to the user with a LabVIEW (National Instruments) program [25]. Knowledge of the generalised coordinates allows the position of the tip to be calculated for each frame using rigid transformations, and an ensemble of such measurements enables visualisation of the volume that the tip is free to explore - the *tip thermal volume* [21]. This is approximately ellipsoidal in shape when the probe is freely trapped, experiencing only optical and thermal forces. Using stereo-microscopy, we estimate that each sphere position is tracked to an accuracy of $\sim$5 nm in x, y and z. Therefore we estimate the tracking accuracy of the tip position to be $\Delta t_x \sim 3$ nm, and $\Delta t_y \sim \Delta t_z \sim 10$ nm (see Appendix for detail of tracking algorithms and error estimations).

3. Probe trapping stiffness calibration

3.1. Background Theory

In this system, the trapping beams interact with non-spherical parts of the probe structure, which will inherently lead to the probe experiencing first order non-conservative trapping forces [26]. However, simulations indicate that non-conservative forces are small (and in fact difficult to measure experimentally) in such a system, until the traps reach the very ends of the trapping

#179434 - $15.00 USD Received 7 Nov 2012; revised 13 Dec 2012; accepted 13 Dec 2012; published 20 Dec 2012
(C) 2012 OSA

cylinders [13]. In this work we are primarily interested in using knowledge of the tip position to elucidate information about a surface it is in contact with, rather than to measure forces. However it is also useful to estimate the force exerted on the sample while in contact with it. This is carried out by applying the analysis described in [21], to calculate the effective trapping stiffness of our probe under different trapping configurations, under the assumption that any non-conservative forces are small and can be neglected.

Equipartition theory can be used to describe the trapping stiffness of an extended optically trapped object [21,27]. In the 1D case, the force f experienced by an optically trapped particle is related to its displacement from equilibrium δx via $f = -K\delta x$ in the linear regime of the trap, where K is the trap stiffness. In the case of our probe, we have 6 degrees of freedom, and the 6×6 element trapping stiffness matrix $\mathbf{K}$ relates the displacements $\mathbf{q}$ to the forces and torques experienced by the probe, $\mathbf{f} = (f_x, f_y, f_z, t_x, t_y, t_z)$, via:

$$\mathbf{f} = -\mathbf{K}\mathbf{q} \tag{1}$$

$\mathbf{K}$ can be calculated in a manner analogous to the simple 1D case by equating the thermal and elastic energy of the system:

$$\tfrac{1}{2}k_B T\mathbf{I} = \tfrac{1}{2}\mathbf{K}\langle \mathbf{q} \otimes \mathbf{q} \rangle \tag{2}$$

here k_B is Boltzmann's constant, T is temperature in Kelvin, $\mathbf{K}$ is symmetric and $\mathbf{I}$ is the 6×6 element unit matrix. $\mathbf{K}$ can therefore be evaluated from an ensemble of measurements of the generalised coordinates $\mathbf{q}$, used to construct the 6×6 element covariance matrix, $\langle \mathbf{q} \otimes \mathbf{q} \rangle$. The element at row i and column j of $\langle \mathbf{q} \otimes \mathbf{q} \rangle$ is given by the covariance term $\langle q_i q_j \rangle$, where q_i denotes the i^{th} element of $\mathbf{q}$. The diagonal terms of $\mathbf{K}$ describe the trapping stiffness in each degree of freedom. The off-diagonal terms describe the stiffness of any coupled motion - allowing force measurements to be recovered from the motion of a coupled system. Such terms can arise when the symmetry of the system is broken by small dissimilarities in the trapping handles or in the optical beams. The correlation matrix $\boldsymbol{C}$ describes the level of coupling between modes, and may be calculated by normalising each element of $\langle \mathbf{q} \otimes \mathbf{q} \rangle$. For example, the correlation between x and y, C^{xy}, is given by $\langle xy \rangle / \sqrt{\langle x^2 \rangle \langle y^2 \rangle}$. We can also use the elements of $\mathbf{K}$ to calculate the location of the *optical stress centre* for the system, the point in space at which coupling is minimised between the modes, and the averaged point about which the probe rotates. This is a useful point to take as the coordinate origin, and it's behaviour as the probe tip comes into contact with a sample surface also enables precise calculation of the contact point, as described in more detail in [21]. In the case of these experiments, the intensity of each trapping beam is equal, and the optical stress centre is located at the centre of mass of the trap positions when it is trapped in free-space.

3.2. Effect of trapping configuration

Here we investigate how the trapping configuration affects the probe's behaviour. Figure 2 indicates how the effective trapping stiffness of translational and rotational modes varies with the separation S between the traps along the sensing axis x (defined in Figs. 1(a) and (b)). The separation of the traps between each side of the micro-tool, D, is held constant and equal to the y-separation of the cylinders in the probe equilibrium frame, throughout these experiments.

The trends in effective trapping stiffness agree with those predicted in [11], and shown experimentally in 2D for a micro-rod in [12]. As expected, the stiffness along the sensing axis, K_x, shows the most pronounced dependence upon trap separation (Fig. 2(a), circles). When the traps are far (over a wavelength) inside the ends of the cylinders, K_x is small. As the beams approach the ends of the cylinders, K_x increases, reaching a maximum when the beams are positioned at approximately half a wavelength from the ends. K_x diminishes as the

#179434 - $15.00 USD Received 7 Nov 2012; revised 13 Dec 2012; accepted 13 Dec 2012; published 20 Dec 2012
(C) 2012 OSA

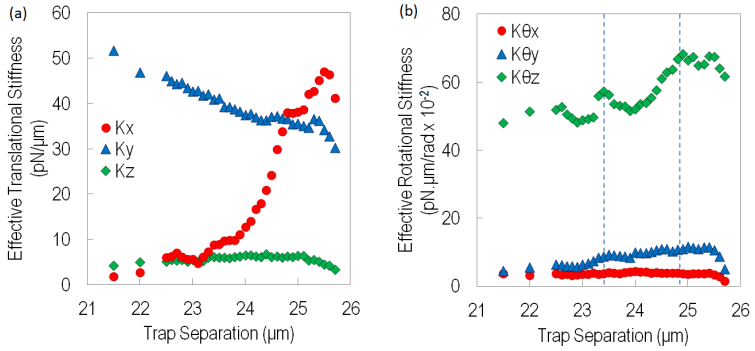

Fig. 2. Variation in the diagonal elements of the stiffness matrix **K** with trap separation S. (a) Translational stiffnesses. The stiffness along the sensing axis x, K_x, is most strongly dependent on trap separation. (b) Rotational stiffnesses. Blue dashed lines indicate the position of peaks in $K_{\theta z}$, for comparison with Fig. 3(d).

beams are further separated after this point, as the beams move off the ends of the cylinders. This behaviour arises because the restoring force along x is dominated by contributions from the end caps of the cylinders; the greatest restoring force is generated when all end caps are simultaneously illuminated by the highest intensity at each beam focus. When the beams are well inside the ends, K_y is the stiffest translational mode. As expected, $K_z < K_y$ due to the elongated shape of the beam focii in the z direction. All components of the translational and rotational stiffness display a reduction as the traps move off the ends of the structure and the probe becomes less stably trapped. The probe was ejected from the optical traps at a separation of 25.8 μm, 100 nm greater than the maximum separation plotted. The elongation of the beam focii also results in $K_{\theta z} < K_{\theta x}$ and $K_{\theta y}$. Figure 2 also shows that $K_{\theta z}$ and $K_{\theta y}$ generally increase with S, since rotation through a given angle about these axes leads to greater displacement of the handles from their equilibrium positions at larger S, which results in greater restoring torques. By the same argument, $K_{\theta x}$ remains constant with increased S, as this is dependent only upon the trap separation along y (D in Fig. 1(b)), which is held constant throughout the experiment.

3.3. Coupled motion

Small undulations in the stiffness - trap separation curves (Fig. 2) reveal detail of the microscopic structure of the trapping cylinders. Subtle departures between the fabricated probe and the desired geometry may result in exaggeration of the coupling between modes. For example, as the structures dry during the fabrication process, the extended struts upon which the cylindrical trapping handles are mounted may undergo a minor bending distortion due to surface tension, as they are only supported at one end of the structure. These distortions are typically small and so not directly visible with optical microscopy. However, observation of how mode coupling varies with trap separation S can give insight into these effects. As described in Section 3.1, **K** is calculated from an ensemble of measurements of the generalised coordinates (**q**) of the probe, enabling force measurements to be recovered from a probe even when it exhibits significant coupling. Figure 3 shows how the off-diagonal elements of the correlation matrix $\boldsymbol{C}$ vary with trap separation. Care must be taken when interpreting these signals as they also contain any systematic coupled measurement errors. However, [21] indicates that coupling errors using our stereoscopic measurement technique are low (in [21],

#179434 - $15.00 USD Received 7 Nov 2012; revised 13 Dec 2012; accepted 13 Dec 2012; published 20 Dec 2012
(C) 2012 OSA

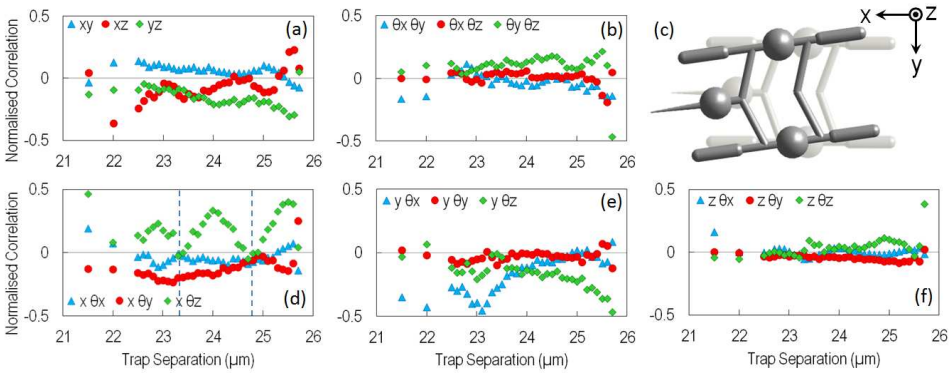

Fig. 3. Variation in the off-diagonal elements of the normalised correlation matrix $\boldsymbol{C}$ with trap separation S. (a) Purely translational correlations. (b) Purely rotational correlations. (c) An example of translational-rotational correlated motion between x and θ_z. *i.e.* when the probe moves forward from its equilibrium position (transparent) along x, it also rotates about z (solid). (d) to (f) Translational-rotational correlations. In (d), $C^{x\theta_z}$ shows oscillations with S, the troughs of which correspond well with peaks in K_{θ_z} (Fig. 2(b)), as shown by dashed blue lines in both cases.

the measured normalised coupling of all modes was found to be < 0.15 in a structure designed to have low coupling), and so we are confident that the relative trends in Fig. 3 are real. Generally, there is an increase in coupling as the trapping beams are moved off the ends of the cylinders and the probe's motion becomes unstable. Of particular note are the oscillations in the coupling between x and θ_z (Fig 3(d), diamonds). We postulate that this could be caused by small undulations in curvature and/or thickness along the length of the trapping cylinders (as the exact location and magnitude of the peaks in the oscillations varies from probe to probe), causing a variation in the level of coupling between x and θ_z as the trap separation S is varied. This effect may also be responsible for the undulations in the rotational stiffness K_{θ_z} (Fig. 2(b), diamonds), and (to a lesser extent) K_x (Fig. 2(a), circles) as the troughs in the x-θ_z coupling coincide with local peaks in stiffnesses K_{θ_z} (indicted by dashed lines) and K_x. This suggests that coupling between two modes reduces the stiffness of each independent mode. However these are minor effects compared to the overall behaviour of stiffness with trap separation.

This section has confirmed that the probe behaves in the 'rod-like' manner as intended, with a stiffness that is maximised when the trapping beams overlap the cylinder ends. For probe transportation across the sample, we require a high trapping stiffness, and so place the trapping beams over the ends of the cylinders. For surface imaging, we place the trapping beams a few microns inside the ends of the cylinders, to achieve a low stiffness (high sensitivity) along the sensing axis (x). This sensitivity can then be controlled by adjusting the trap separation, while leaving the pointing precision of the tip relatively unaffected. The design of our probe gives it additional advantages over an optically trapped micro-rod: the spherical tracking points allow more accurate measurement of position and orientation than shown in [12] (see Appendix), and the trapping beams are removed from the probe tip, minimising sample illumination and problems due to beam occlusion. We now go on to show how the performance of the probe can be further enhanced by position clamping specific modes of its motion.

#179434 - $15.00 USD Received 7 Nov 2012; revised 13 Dec 2012; accepted 13 Dec 2012; published 20 Dec 2012
(C) 2012 OSA

4. Position and rotation clamping

By reducing the trapping laser power, we linearly reduce the trapping stiffness of all modes within the stiffness matrix [21]. Hence the sensitivity of the probe is increased along the sensing axis, x, but at the expense of the pointing precision of the tip - *i.e.* the tip also explores a larger region of space along y and z. Position clamping of selected modes offers a method of improving the pointing precision of the tip at a lower laser power without affecting the sensitivity [20]. It is achieved by measuring the particles displacement from equilibrium (for example Δx), and responding by moving the traps a distance $G \times \Delta x$ (where G is a negative gain factor) in the opposite direction, to exert a larger force pulling the probe back towards its equilibrium position. The quality of the position clamping is dependent upon the reaction time between position measurement and trap update, and the refresh rate of the spatial light modulator. In our system the maximum refresh rate of the spatial light modulator is 203 Hz, and the maximum camera frame rate over the required region of interest is 1 kHz with an integration time of 1 ms. The reaction time from measurement of probe position to trap movement is $\sim$10 ms - more details of this are discussed in [23]. These time delays limit the maximum stiffness attainable with closed-loop control. Provided that the relevant delays are smaller than the relaxation times of the system, the magnitude of the clamping gain coefficients can be increased beneficially. However, when the two times scales become similar in size, increasing the gain further can result in weaker clamping and, ultimately, in instability [28]. Within these constraints, we are able to position clamp the four least stiffly trapped modes (translations in x and z, and rotations about x and y) of our probe's motion. Translations in y and rotations about z are already too stiffly trapped to position clamp with our system. Optimum gains for each mode are first determined by measuring the effective stiffness at increasing gain

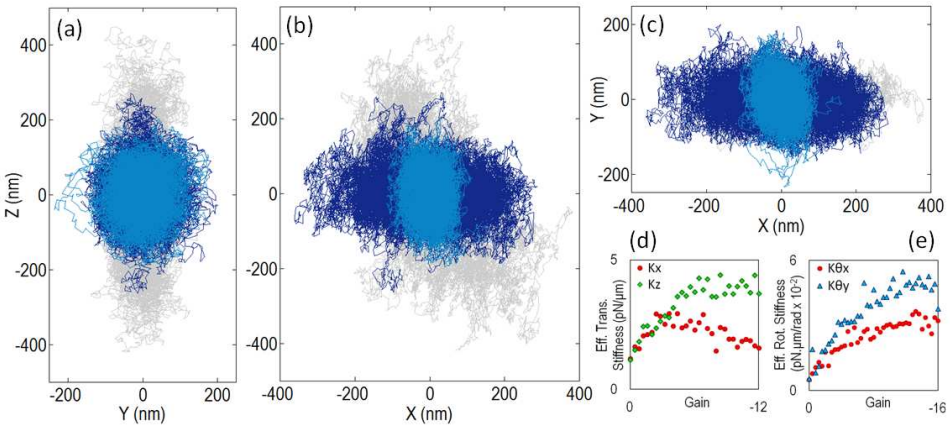

Fig. 4. The tip thermal volume under different clamping conditions. (a), (b) and (c) show the tip trajectory viewed along x, y and z-axes respectively, under 3 different clamping conditions. Light grey shows the unclamped trajectory. Light blue shows the trajectory when clamped in all possible modes (x, z, θ_x and θ_y). Dark blue shows the trajectory when clamped in z, θ_x and θ_y, yielding a high sensitivity (large variance) along the sensing axis x, but retaining good pointing precision (low variance) in transverse directions. (d) and (e) show the effective stiffness of these modes under increasing gain magnitude, allowing the gain to be chosen to maximise the stiffness of the desired mode. As the optimum gain peaks are broad, they are robust to any small structural differences between probes, and therefore once optimum gains have been found for a single probe they will give near optimum results for other probes too.

#179434 - $15.00 USD Received 7 Nov 2012; revised 13 Dec 2012; accepted 13 Dec 2012; published 20 Dec 2012
(C) 2012 OSA

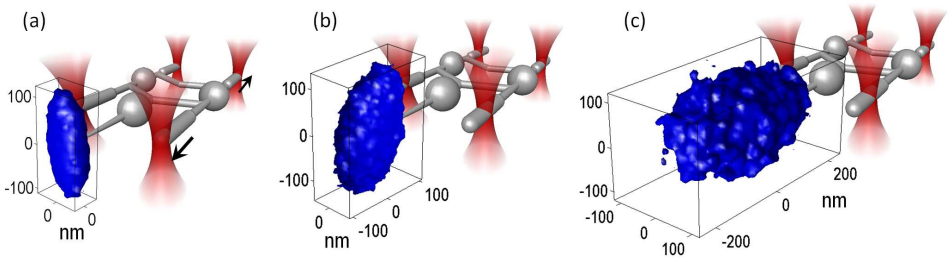

Fig. 5. Controlling the shape of the tip thermal volume. (a) The trapping stiffness is maximised when the traps overlap the end caps of the cylindrical handles, therefore yielding the smallest tip thermal volume. (b) The traps are positioned 3 μm inside each end of the cylinders. (c) The same trapping configuration as (b), but with the trapping power reduced by $\sim 50\%$, and modes z, θ_x and θ_y clamped. The tip thermal volumes shown are exaggerated by a factor of 60 in each case relative to the probe sketch, for clarity.

magnitudes until instability begins to set in, and the effective stiffness begins to fall. Example curves are shown in Fig. 4(d) and (e). The optimum gains will depend on the exact trapping configuration and power used during a particular experiment. Figure 4 shows the spread of tip positions under different combinations of mode clamping, viewed along the x (a), y (b), and z (c) axes respectively. The light grey line shows the tip trajectory with no feedback. The light blue trace shows the effect of clamping in all possible modes, significantly reducing the variance of the probe tip. The dark blue trace shows the trajectory of the tip when the probe is clamped in z, θ_x and θ_y, yielding a high sensitivity (large variance) along the sensing axis x, but retaining good pointing precision (low variance) in transverse directions.

By adjusting the trapping configuration, and selectively clamping specific modes, we change the effective trapping stiffness, and also radically alter the shape of the tip thermal volume. Figure 5 shows smoothed outer surfaces of the region the tip is free to explore under a range of conditions. (a) shows the tip thermal volume when the traps overlap the ends of the trapping cylinders, (b) shows how it is expanded when the traps are positioned 3 μm inside each end of the cylinders, and (c) shows it when using the same trapping configuration as (b), but with the trapping power reduced by $\sim 50\%$, and modes z, θ_x and θ_y clamped (the same conditions as shown in Fig. 4(a), (b) and (c), dark blue line). All tip thermal volumes are exaggerated by a factor of 60 in size relative to the probe sketch for clarity. Without clamping, we would expect the volume in Fig. 5(c) to be an enlarged (each dimension $\sim\times\, 2$) version of 5(b), maintaining the same aspect ratio. However, position clamping of the chosen modes compresses the tip motion in z, increasing the tip's pointing precision. It is useful to measure the pointing precision by considering the width and height of the tip thermal ellipsoid, which is characterised using the standard deviation of the spread of tip positions along y and z, $\sigma_{y,tip}$ and $\sigma_{z,tip}$ respectively. In Fig. 5(c), $\sigma_{y,tip} = 48$ nm and $\sigma_{z,tip} = 58$ nm. The sensitivity of the probe is best characterised by its trapping stiffness along its sensing axis x. Since motion of the probe tip in this direction is purely translational in origin [21], $K_{x,tip} = K_x \approx 3.5 \times 10^{-7}$ N/m, for the conditions shown in 5(c). This estimate of the spring constant in the sensing axis of our shaped particle is similar in magnitude to that demonstrated in [29], in an experiment designed to measure ultra-low forces using an optical trap.

Using a combination of handle shaping and position clamping we have produced a probe which is highly sensitive in the sensing axis x, and therefore exerts a low average force on

#179434 - $15.00 USD Received 7 Nov 2012; revised 13 Dec 2012; accepted 13 Dec 2012; published 20 Dec 2012
(C) 2012 OSA

samples during scanning, but maintains a good pointing precision, allowing the location of the interaction with the sample to be well defined. In the next section we investigate and refine the manner in which our probe interacts with a sample surface.

5. Force clamping and measurement of surface topography

We now demonstrate the use of our sensor as a low force surface topography probe. In addition to position clamping to achieve a good pointing precision at high force sensitivity, we also apply a force clamping technique along the sensing axis, x, to ensure the probe maintains contact with the sample during the scan at a constant average force. In contrast to position clamping, force clamping updates the trap positions not to return the probe to its equilibrium position, but to maintain it at a constant displacement from equilibrium, thus exerting a constant average force on the sample. Here we use a closed-loop algorithm that simultaneously position clamps the probe in modes z, θ_x and θ_y, force clamps the probe along its sensing axis x, and automatically scans the probe laterally (parallel to y) to measure a surface profile. The performance of our probe is tested on a calibration sample, also fabricated using direct laser writing, and shown in Figs. 6(d), (e) and (g). It presents a vertical surface with steps of increasing depth along one side, each separated by 1500 nm. The opposite side of the calibration grid presents a series of grooves of varying width.

We initially trap the probe adjacent to the sample, as shown by 'left' and 'right' eye stereo views in Fig. 6(f). The trajectory of the tip throughout a scan is shown in Fig. 6(a), viewed along the z axis. When the scan is initiated, the probe moves forwards (in the x-direction) until its displacement in the sensing axis, x, reaches a desired set point. The force clamp is maintained as the probe is then scanned laterally along the sample parallel to the y- axis, over steps of 100, 200 and 500 nm in depth. The front edge of the trajectory plot reveals the surface, here represented by the red line. Rather than simply tracing the edge of the recorded trajectory, this line is reconstructed by separating the data into sections based on y position, and averaging the front most portion of each section. This method was chosen to reduce the impact of individual parts of the trajectory that encroach inside the surface due to any tracking errors.

The inset shows the trajectory of the tip as the probe scans over smaller steps (40, 50, 60, 70, 80, 90, 100, and 200 nm in depth). In Fig. 6(b), the horizontal axis has been compressed relative to the vertical axis to more clearly reveal the steps. The measurement of the tip position is made in three dimensions, which is important to determine the position of the tip correctly. However, here we present a two dimensional view of the tips trajectory, as the vertical third dimension of the calibration grid does not vary. The standard deviation in the difference between the step size of the calibration grid design, and the measured step size here, is 11 nm, allowing us to estimate the accuracy of the depth measurement of our scan. This is a worst case estimate, as it is made under the assumption that the calibration grid is perfectly fabricated. The trapping power and configuration used in these scans was identical to those described for Fig. 5(c), and the force clamp set point used was 400 nm, resulting in an estimated average force normal to the surface under investigation of 3.5×10^{-7} N/m $\times 400$ nm = 140 fN during the scan. The lateral scan-speed used in these cases was 50 nm/s.

There is a simple relationship to consider when selecting the scan-speed to successfully image the surface. The lateral scan-speed, v_{lat}, required to allow the probe long enough to fully investigate each part of the surface as it passes over, is dependent upon the width and height of the tip thermal volume (characterised by $\sigma_{y,tip}$ and $\sigma_{z,tip}$ respectively, as described in Section 4), and the time it takes to investigate this volume (characterised by the relaxation times of motion in these directions, $\tau_{y,tip}$ and $\tau_{z,tip}$). Considering the first case, $v_{lat} \propto \sigma_{y,tip}/\tau_{y,tip}$, where $\sigma_y = \sqrt{(k_B T/K_{y,tip})}$, and $\tau_{y,tip} \propto 1/K_{y,tip}$. Here k_B is Boltzmann's constant, T is temperature in Kelvin and $K_{y,tip}$ is the lateral stiffness of the probe tip. Combining these we see

#179434 - $15.00 USD Received 7 Nov 2012; revised 13 Dec 2012; accepted 13 Dec 2012; published 20 Dec 2012
(C) 2012 OSA

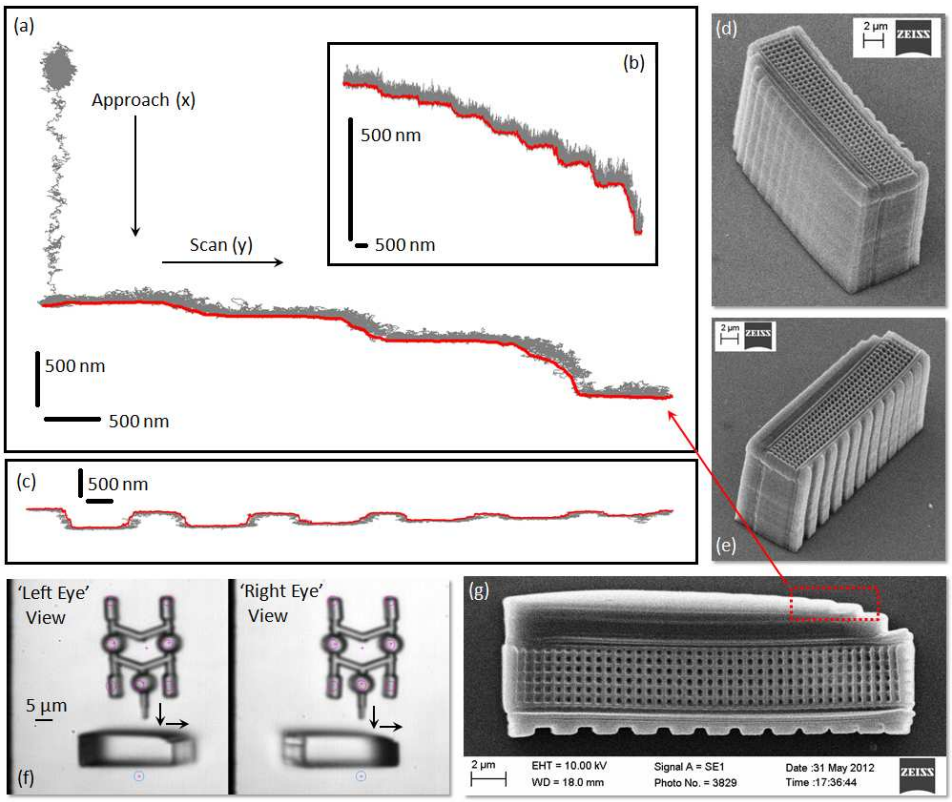

Fig. 6. Measurement of the surface topography of a test sample. (a) The trajectory of the probe tip (grey line) as it approaches the sample, and then scans laterally over steps of 100, 200 and 500 nm in depth. The red line indicates the measured interface. (b) A scan over shallower steps (40, 50, 60, 70, 80, 90, 100, and 200 nm in depth) to test the height resolution. In (b) the horizontal axis has been compressed to more clearly reveal the steps, the scale bars show the relative scaling along each axis. (c) A scan over corrugated part of another test sample, similar to that shown in (e). All scale bars on (a), (b) and (c) represent 500 nm. (d), (e), and (g) are scanning electron microscope images of the test sample. (f) 'Left eye' and 'right eye' stereo-microscope images of the probe held adjacent to the test sample prior to the start of the experiment.

that $v_{lat} \propto \sqrt{K_{y,tip}}$. A similar argument holds for the vertical stiffness of motion of the tip $K_{z,tip}$. Therefore, to optimise imaging speed, it is useful to ensure that modes which contribute to $K_{y,tip}$ and $K_{z,tip}$ are as stiff as possible. $K_{y,tip}$ is dependent upon K_y and $K_{\theta z}$, and the probe's handle geometry ensures these modes are already relatively stiff (Fig. 2). $K_{z,tip}$ is dependent upon K_z and $K_{\theta y}$, which are stiffened by position clamping as shown in Section 4. Therefore, by shaping the probe handles, and position clamping the motion of selected modes, we not only increase the pointing precision, but also increase the rate at which surface topography can be imaged. These relationships also indicate that the scan-speed may be increased by reducing the relaxation times of the motion of the tip ($\tau y,tip$ and $\tau z,tip$). This may be achieved by reducing the overall size (such as tip length and handle separation) of the probe. As with other scanning probe techniques, slower scans ensure higher resolution (within the other limits discussed here), and the scan rate can be further optimised depending upon the desired imaging quality. Unlike other scanning probe techniques, using this method allows the number of probes

#179434 - $15.00 USD Received 7 Nov 2012; revised 13 Dec 2012; accepted 13 Dec 2012; published 20 Dec 2012
(C) 2012 OSA

operating simultaneously to be readily increased, decreasing the time taken to image a given area.

6. Conclusions

In this work we have combined the ultra low force capabilities of optical tweezers with a scanning probe approach, to investigate the use of an optically actuated shaped particle as a surface topography sensor. Using direct laser writing, we have fabricated an extended probe which is multiply trapped and controlled using holographic optical tweezers. We have specifically shaped the handles of our probe to generate 'rod like' behaviour, in that the trapping stiffness anisotropy is strongly dependent upon trapping configuration in a manner similar to that of a multiply optically trapped micro-rod. This enables the probe's sensitivity and tip pointing precision to be controlled by varying the relative positions of the trapping beams. The probe's three dimensional position and orientation is measured in real-time at up to 1 kHz using high-speed video tracking of stereo-microscopic images. We estimate the tracking accuracy of the tip in each direction to be $\Delta t_x \sim 3$ nm, and $\Delta t_y \sim \Delta t_z \sim 10$ nm (see Appendix for details). The performance of the probe is further enhanced by position clamping specific modes, lowering the force exerted on the sample and potentially increasing the rate that the surface can be successfully scanned.

To test our probe, we scan it laterally over a calibration sample consisting of a series of graduated steps, and demonstrate a height resolution of ~ 11 nm along the sensing axis x, normal to the surface under investigation. The lateral (y) and vertical (z) resolution of the imaging technique is limited by the radius of curvature of the tip, which in this case is 100 nm laterally and 300 nm vertically. By fabricating probes with sharper tips, for example by using a focused ion beam, or electron beam lithography, as employed in [30], this limitation could be overcome and this technique could be used to delicately image samples with full 3-dimensional nano-scale resolution.

We use equipartition theory to estimate the forces exerted on the sample during imaging, and apply force clamping to maintain a constant average force of 140 fN on the sample throughout a scan. This force is ~ 4 orders of magnitude lower than average force exerted in standard contact mode atomic force microscopy, and also compares favourably to the forces exerted in the 'non-contact mode atomic force microscope', a scanning probe technique designed specifically to exert exceptionally low forces [31].

An additional advantage of our probe geometry is that the optical traps are spatially separated from the tracking spheres and therefore act as a crude 'optical shield' around the tracking points [32,33], preventing small particles and detritus (that can be present in more challenging biological environments) from producing erronius tracking signals. Although detritus trapped alongside the probe is obviously to be avoided, in this case it will only affect the trapping behaviour, not the coordinate measurement. This situation is tolerable for the imaging application demonstrated here, as we are primarily interested in using knowledge of the tip position to elucidate information about a surface it is in contact with, rather than accurately measure forces.

In summary, we have developed an ultra low force scanning probe technique, which uses an optically actuated shaped probe, allowing strongly scattering samples to be imaged from any arbitrary direction. The extended nature of the design removes the trapping beams from the interface under investigation and minimises problems due to beam occlusion. We anticipate that this technique may be used to image the surfaces of non-motile cells resting on, or adhered to, a substrate. For example, the green alga *Pseudopediastrum boryanum* has previously been imaged, at a lower resolution, using a similar technique [19]. The combination of the features presented here make our technique ideal for obtaining high resolution images of soft biological

#179434 - $15.00 USD Received 7 Nov 2012; revised 13 Dec 2012; accepted 13 Dec 2012; published 20 Dec 2012
(C) 2012 OSA

specimens such as this, that would otherwise be disturbed or damaged.

Appendix

Additional tracking details

The probe *equilibrium frame* is first established by calculating the average of each tracking sphere position over an ensemble of coordinate measurements. The probe equilibrium frame has an origin defined as the mean position of each averaged sphere position, its x-axis points from the origin to the mean position of sphere A (with the tip protruding from it), and its z-axis is orthogonal to the plane defined by the mean position of the three spheres. For small angles (such as rotations due to Brownian fluctuations), we can ignore the non-commutability of the rotation matrices and describe the probe's orientation in terms of three separate rotations, θ_x, θ_y and θ_z, about the axes defining the probe equilibrium frame. Once the generalised coordinates $\mathbf{r}$ and θ are known, the coordinates of the probe tip ($\boldsymbol{t} = [t_x, t_y, t_z]$), positioned at vector $\boldsymbol{v}$ from the origin of the current probe frame, are calculated using $\boldsymbol{t} = \mathbf{r} + \boldsymbol{A}^{\Omega} \cdot \boldsymbol{v}$, where $\boldsymbol{A}^{\Omega}$ is the rotation matrix defining the rotation from the equilibrium frame to the current orientation.

Estimation of tracking accuracy

We have access to two signals that allow us to estimate the tracking accuracy of our probe:

1). Ideally, both left and right images should measure the same displacement in the lab. y direction (parallel to the vertical sides of the camera image shown in Fig. 6(f)), and any departure from this can be used as an error signal. We calculate the relative displacement in y between successive frames in both 'left' and 'right' images. For each tracking point independently, we calculate the RMS difference in an ensemble of these measurements to estimate the error in the tracking in the y-direction [24].

2). The errors in measurements of lab. x and z may be larger than those in y as the image is blurred in this direction by the off-axis illumination. A second method to estimate tracking errors takes into account contributions from measurements in all three dimensions, relying on the fact that we are observing an extended rigid particle. Ideally we would expect the measured distance between handles to be constant, as the probe translates and rotates in 3D due to Brownian motion. Calculation of the standard deviation of measured distances between the handles from frame to frame provides another way to estimate tracking errors, including contributions from all degrees of freedom.

Both of these error signals are calculated and displayed in real time during an experiment, allowing them to be minimised by adjustment of the illumination system during the set-up phase. They also serve as an immediate warning if the tracking quality degrades during an experiment. In the experiments presented here, it was possible to minimise 1). to $\sim< 3$ nm, and 2). to $\sim< 5$ nm. We therefore use ~ 5 nm as a worst case estimate of measurement accuracy of the position of each handle in each dimension (Δh).

By error propagation we can then estimate the accuracy of the probe's centre of mass position (taken as the centre of the three tracking spheres), Δx, Δy and Δz. The probe's x-position is calculated using $x = (A_x + B_x + C_x)/3$, where A, B and C identify the three tracking spheres, and A_x defines the x-coordinate of sphere A. We assume $\Delta A_x = \Delta B_x = \Delta C_x \sim \Delta h$. The estimated error in x is therefore $\Delta x = \Delta h/\sqrt{3}$, by propagation of errors. Therefore, when $\Delta h \sim 5$ nm, $\Delta x \sim 3$ nm. Similarly $\Delta y \sim 3$ nm and $\Delta z \sim 3$ nm.

The measurement accuracy of the motion of the probe tip $\boldsymbol{t} = [t_x, t_y, t_z]$ can be estimated with reference to Fig. 7. There is no rotational contribution to t_x [21], therefore $\Delta t_x = \Delta x \sim 3$ nm. However, Δt_y and Δt_z depend rotations and the geometry of the probe - namely the tracking

#179434 - $15.00 USD Received 7 Nov 2012; revised 13 Dec 2012; accepted 13 Dec 2012; published 20 Dec 2012
(C) 2012 OSA

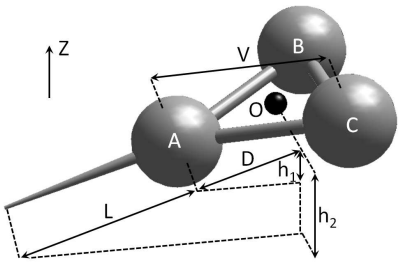

Fig. 7. Probe geometry for estimation of the accuracy of tip position measurement. Tracking spheres A, B and C are on the vertices of an equilateral triangle of side length V. The black sphere O represents the centre of the triangle, a distance D from each vertex. The probe tip length is L. In the analysis, we assume L and V are fixed, known constants. L for a particular probe can be calculated as described in [21], and V is taken as the average separation between tracking spheres.

sphere separation V and tip length L. The errors in these coordinates are estimated as follows: $h_2/(L+D) = h_1/D$, where $h_1 = O_z - A_z$, $h_2 = (L+D)(O_z - A_z)/D$ and $O_z = (A_z + B_z + C_z)/3$. By assuming that the handles are on the vertices of an equilateral triangle of side length V, therfore $D = V/\sqrt{3}$, and

$$t_z = O_z - h_2 = \left(\frac{2L}{\sqrt{3}V} + 1\right) A_z - \left(\frac{L}{\sqrt{3}V}\right) B_z - \left(\frac{L}{\sqrt{3}V}\right) C_z \tag{3}$$

therefore by propagation of errors, assuming no correlation and fixed L and V:

$$\Delta t_z = \left[\left(\frac{2L}{\sqrt{3}V} + 1\right)^2 + 2\left(\frac{L}{\sqrt{3}V}\right)^2\right]^{\frac{1}{2}} \Delta h \tag{4}$$

In the case of our probe, $V \sim 12\ \mu$m and $L = 10\ \mu$m, therefore $\Delta t_z \sim 10$ nm. A similar argument also yields $\Delta t_y \sim 10$ nm. Equation 4 can be considered at the probe design stage to ensure that the chosen geometry (specifically L and V) yields the desired tip tracking accuracy. If necessary, the tracking accuracy could also be further improved by increasing the number of tracking points on the probe.

Acknowledgments

This work is funded through an Engineering and Physical Science Research Council Grant (United Kingdom). It was carried out with the support of the Bristol Centre for Nanoscience and Quantum Information. We are very grateful to Professor John Rarity for the use of the Nanoscribe *Photonic Professional* direct write laser lithography system for probe fabrication. We would also like to thank Dr. James Grieve and Michael Lee for useful discussions. MJM and MJP acknowledge a Royal Society Wolfson Merit Award.

#179434 - $15.00 USD Received 7 Nov 2012; revised 13 Dec 2012; accepted 13 Dec 2012; published 20 Dec 2012
(C) 2012 OSA